FLIGHT DYNAMICS OF SMALL VEHICLES

Steven Ho[1*], Hany Nassef[1], Nick Pornsin-Sirirak[2], Yu-Chong Tai[2], Chih-Ming Ho[1]
[1]Mechanical and Aerospace Engineering Department, University of California Los Angeles
[2]California Institute of Technology
[*]email: hos@ucla.edu

Keywords: *unsteady aerodynamics, micro air vehicles, active flow control, MEMS*

Abstract

Experimental studies of both the unsteady aerodynamics of micro air vehicles [MAVs] utilizing flapping wings and various active flow control strategies for flexible aerodynamic surfaces are described. Flow visualization and lift and thrust measurements clearly show that a stable unsteady leading edge vortex and its interaction with the stiffness distribution of a flapping wing determine the aerodynamic performance of the MAV. Two active flow control strategies, one for local vortex control using electrostatically controlled checkvalve actuators fabricated directly on the wing, and the other involving instantaneous variation of the wing's angular speed to achieve global vortex control, are also presented. Combined with a novel distributed control algorithm (the Gur Game), they light a path toward adaptive flow control of flexible surfaces.

1 Introduction

Motivation for this study stems from recent interest in very small payload carrying flight vehicles. Such vehicles would be useful for remote sensing missions where access is restricted due to various hazards. These vehicles have a typical wingspan of 15 cm, with a weight restriction of less than 100g [1]. The goal is to consider a flapping wing design as a novel approach to the problem, since the size and speed range of the vehicle closely matches small birds and insects, which are obviously very capable fliers.

It has long been realized that steady state aerodynamics does not account for the actual forces produced by natural fliers, and this prompted several studies [2][3][4] on the unsteady flow produced. Mechanisms such as rotational circulation, wake capture, and the unsteady leading edge vortex do seem to properly account for the necessary aerodynamics forces. Regarding forward flight, the unsteady leading edge vortex is the only mechanism present to account for the necessary forces. The unsteady leading edge vortex involves leading edge flow separation that reattaches to the wing and forms an attached vortex bubble. This vortex helps increase the circulation on the wing and account for higher than normal (steady) forces. This vortex is stable due to it's highly three dimensional nature [5].

Flow control measures to increase lift and thrust for mechanical flapping flight remains a relatively unexplored arena. Much work has been done on natural fliers and their methods of increasing lift, but there is a dearth of research for artificial fliers. Yet the unsteady flow field and the tight aeroelastic coupling between the wing deformation and the surrounding fluid offers great hope that small actuators placed at the right positions, and with an appropriate feedback controller, could lead to large gains in aerodynamic performance with relatively modest power inputs. The main challenges involved would then be fabricating the actuators in line with the weight constraints and selecting the appropriate feedback controller for such a highly nonlinear system.

2 Experimental setup

This work was conducted in a small wind tunnel facility at the University of California, Los

Angeles. The tunnel test section measured $30 \times 30 \times 60$ cm and had an inlet contraction ratio of 4:1. The speed range in the tunnel was 0-10 m/s, with most experiments being conducted between 3-4 m/s. The flow uniformity over the entire speed range of the tunnel was found to be 0.5%. The test section was modified to allow for smoke wire visualization using an 80 μm diameter chromium wire that was electrically heated with 3 amps. A mixture of mineral oil and aluminum powder periodically dripped on the wire to produce the smoke. Due to flow cooling of the wire, visualization was possible at speeds at or below 1 m/s. Load cells of 150g and 100g capacity took unsteady force measurements of lift and drag, respectively. A 16-bit resolution ADC board allowed for minimum force resolution measurements of 33 mg for lift and 24 mg for drag. The ADC board had two analog output channels that powered the load cells and the vehicle's dc motor. A specially written LABVIEW 5.0 routine automated the entire setup. Figure 1 shows the experimental setup.

Figure 1: Wind tunnel and test stand load cells

In order to perform the aerodynamic tests, a simple, lightweight flapping device had to be designed and built. The flapping cycle is intimately linked to the transmission design, and often does not mimic the natural cases of bird or insect wing motion. The transmission (see Figure 2) allowed us to test the effects of flapping amplitude, frequency, stroke plane inclination, and feathering angle. Two transmission heads were built with flapping amplitudes of 60° and 90°. A 6mm diameter Namiki electric vibrator motor drove the transmission. The motor nominal voltage is 1.3V with a stall torque of 0.8 g-cm. The motor operated at up to 6V and geared 24:1 to provide sufficient torque to drive the wings. With this motor the maximum flapping frequency was 15 Hz for the 90° flapper and 30 Hz for the 60° flapper. Stroke plane inclination effects could be studied since the flapper mount could be angled up to +/-45° with respect to the horizontal. The feathering angle, defined as the angle between the wing chord line and the stroke plane, could be varied by rotating the wing about its shaft and tightening a set screw.
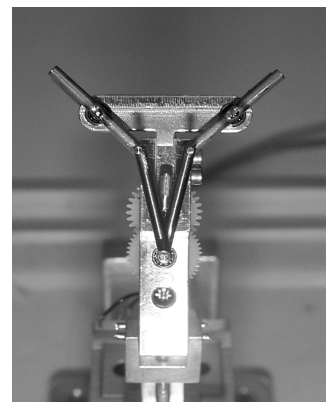

Figure 2: Flapping wing transmission

3 Passive wing aerodynamics

3.1 Stiffness distribution effects

Figure 3 shows the wind tunnel test results of rigid cicada wings and flexible titanium-alloy wings without the support of carbon fiber rods at the leading edges. It demonstrates that spanwise stiffness is an important factor in lift production in flapping flight. For the same size of wings, cicada wings with rigid leading edges produced larger lift coefficients compared to wings having flexible leading edges, with the lift increase rising rapidly as the unsteadiness increases. In the regime of advance ratio less than one, i.e., unsteady flow, the lift coefficients of wings with rigid leading edges increase rapidly while that of flexible leading edges loses lift.

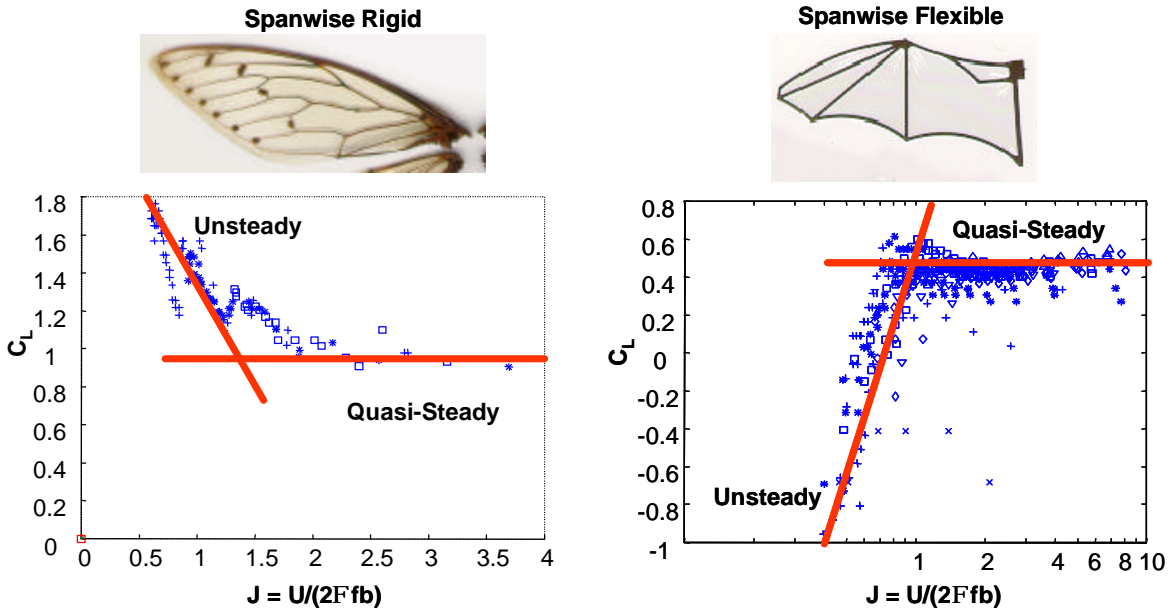The aerodynamic lift and thrust coefficients can be expressed as follows:

Spanwise Rigid

Spanwise Flexible

Figure 3: Stiffness distribution effect on lift performance

$$C_L = \frac{L}{\frac{1}{2} r U^2 A}, \quad C_T = \frac{T}{\frac{1}{2} r U^2 A} \qquad (1)$$

where L, T, U, A, and r are lift, thrust, flight speed, wing planform area, and air density, respectively. The advance ratio, J, is the ratio of the flight speed to the speed of the wing tip and is given by:

$$J = \frac{U}{2\Phi f b} \qquad (2)$$

where F, f, and b are flapping amplitude, flapping frequency, and wing semi-span, respectively. Typically, unsteady state flight has an advance ratio of J less than 1. For example, natural fliers such as a bumblebee, black fly, and fruit fly have an advance ratio in free flight of 0.66, 0.50, and 0.33, respectively.

Stiffness distribution also plays a large role in thrust production because of the tightly coupled aeroelastic nature of the system. Any change in the manner of wing deformation will cause a change in the aerodynamic performance and vice versa. This coupling is especially strong when dealing with thrust generation. This is likely due to the dependence of thrust production on vortex shedding from the wing

during the upstroke. Hence, modifying the stiffness distribution will change the wing deformation and therefore the vortex shedding characteristics. Two identical wings were tested and compared according to the C_T. One wing has a paper membrane while the other has a Mylar membrane. The paper membrane is less flexible than the Mylar wing due to the higher stiffness of paper. As seen in Figure 4, the thrust performance differs greatly and it diverges faster as the advance ratio decreases. This shows clearly the importance of achieving the proper stiffness distribution for maximum aerodynamic performance.
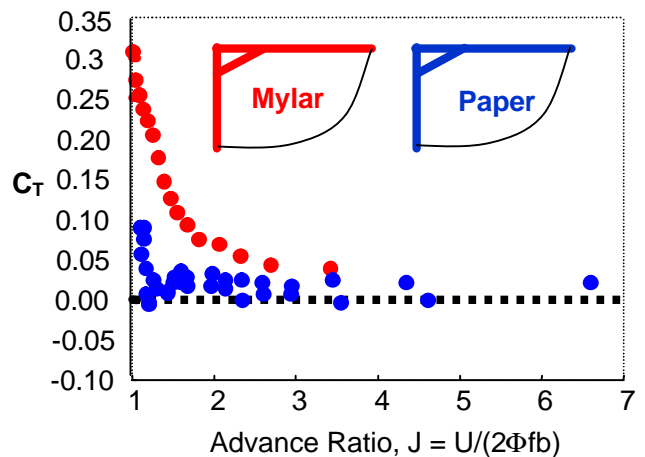

Figure 4: Stiffness effect on thrust production

3.2 Unsteady leading edge vortex

Smoke wire flow visualization in Figure 5 (selected streamlines are highlighted for clarity) shows the formation of a leading edge separation bubble during the downstroke. At the start of the downstroke, the flow stagnates at the leading edge of the wing. The stagnation line progressively moves to the upper surface of the wing, thereby by forming a leading edge vortex. This vortex grows and attains its maximum size near the middle of the downstroke.
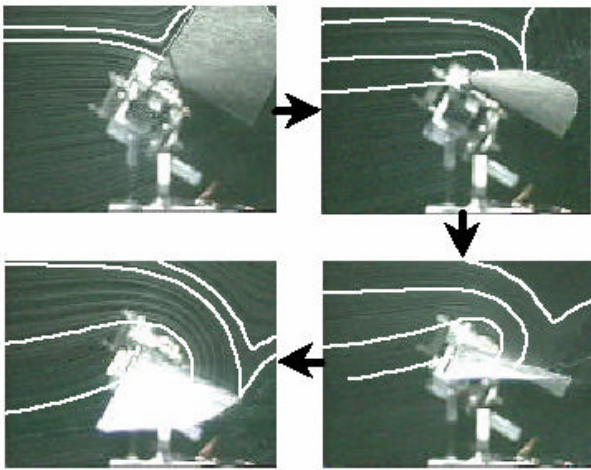

Figure 5: Leading edge vortex separation

This vortex finally sheds at the start of the upstroke. Previous work by Van Den Berg and Ellington [5] and this current study notes that this leading edge vortex is accompanied by a strong outward spanwise flow (see Figure 6). The spanwise flow helps stabilize the vortex in the midspan section of the wing through vortex stretching. The spanwise flow decelerates towards the tips and the vortex core can be seen to increase.

The size of the unsteady leading edge vortex was observed to depend on the advance ratio, J. For large advance ratios ($J > 1$, quasi-steady flow), no vortex was seen and the flow was always attached. However, as the advance ratio decreased below unity (unsteady flow), the unsteady leading edge vortex appeared regardless of the chord size of the wing. For $0.25 < J < 0.5$, the diameter of the unsteady

leading edge vortex was 3-4 cm near the midspan region.

Figure 6: Spanwise flow

The low pressure region created by the unsteady leading edge vortex accounts for the lift produced on the wings. As the vortex is shed, the lift force decreases and is negative during the upstroke. Previous studies corroborate these results and further prove that the lift force is primarily produced during the downstroke with its maximum being located near mid-downstroke [6][7]. The negative lift portion is attributed to a vortex that forms underneath the wing during the upstroke that is smaller than the unsteady leading edge vortex formed on the upper surface.

3.3 Thrust generation

For the first time the effect of the inboard and outboard region in relation to thrust and lift generation has been identified. Figure 7 depicts the effect. Two wings were compared where the inboard region of one wing was arbitrarily removed. Since the wing speed varies along the span, the strength of the unsteady leading edge vortex will also vary and thus the lift. The rotational speed of the wings is higher toward the tips and leads to stronger amounts of vorticity in the outboard region of the wings. Therefore, it can be expected that the bulk of the lift is produced in the outboard region of the wings. Remove of the inboard region did not
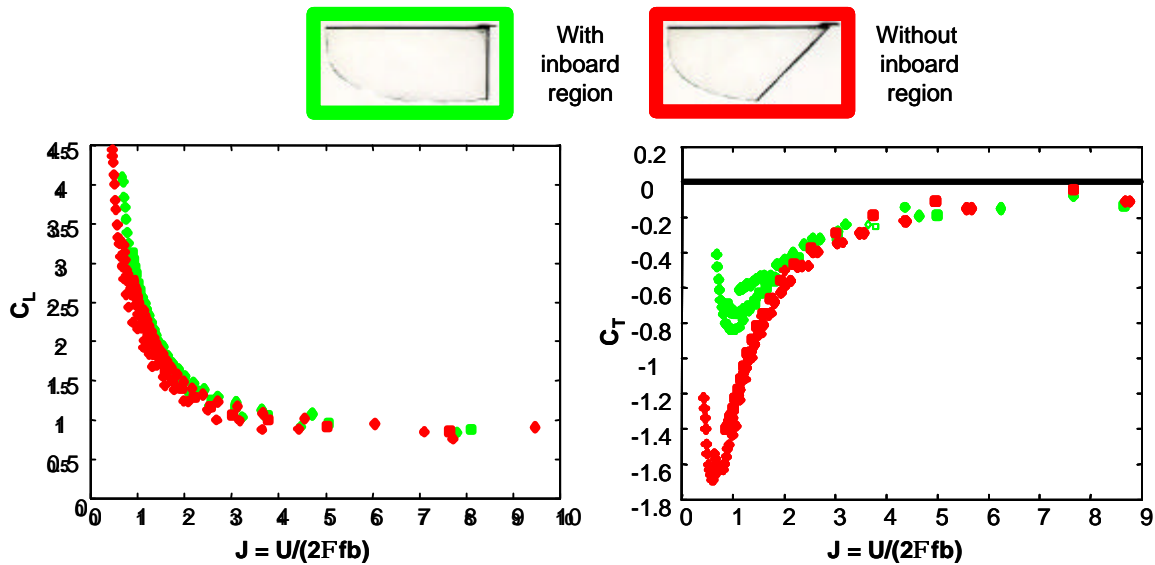
Figure 7: Effect of inboard region on thrust production

affect the lift coefficient, as shown in Figure 7 because the outboard vorticity was not affected. However, the thrust production was influenced. The thrust performance of the wing without the inboard region deteriorates when compared to that of the wing with the inboard region, which is yet another indication of the dependence of thrust on the vortex shedding.

It is believed that the thrust production is intimately tied with the vortex shedding. Figure 8 shows an example of the unsteady thrust measurements.
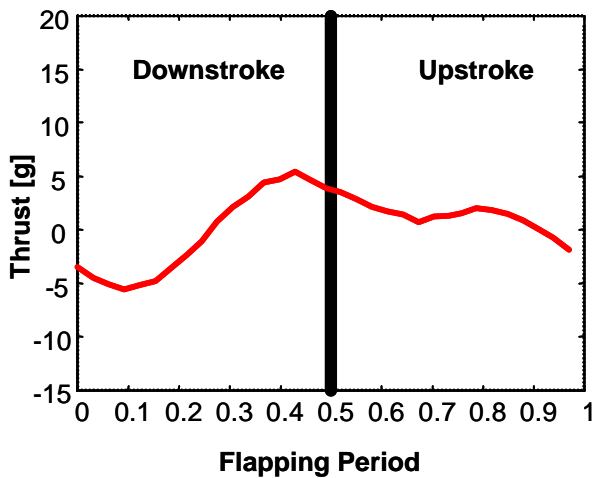

Figure 8: Typical thrust generation phase average

Notice that thrust is not produced until the later part of the downstroke and well into the upstroke, a time where the unsteady leading edge vortex is being shed according to the flow visualization. Any wing can produce an unsteady leading edge vortex of some strength and thereby a fixed amount of lift; however, depending on the wing's flexibility and orientation, that vorticity could be shed differently, leading to different thrust generation.

4 Active wing flow control

There exists a wealth of research on flow control techniques for separated flows. Past researchers have used suction, blowing, or some combination thereof [8][9] to control the leading edge vortices found atop delta wings. Inertial and engineering constraints on mechanical flapping wings, however, prohibit complicated and relatively heavy pneumatic lines for suction or blowing. The advent of microelectromechanical systems [MEMS] technology, however, offers a way to manufacture microvalve actuators comprised entirely of thin layers of parylene and gold. These actuators can be directly fabricated on the wing membrane, electrically actuated, and add virtually no inertial load since they are only a few microns thick.

4.1 Distributed MEMS actuators

MEMS wings integrated with an active checkvalve electrostatic actuator parylene skin are shown in Figure 9 and close up photographs of the actuators individually and in array format are seen in Figure 10. The checkvalves feature vented through holes with tethered parylene caps on the skin to rectify the airflow in one direction. Each vent hole is covered by a tethered valve-cap with a diameter of 500 μm and 900 μm, respectively. Two metal layers are added for ground and high voltage contacts to form to electrodes, which will attract each other under an applied voltage. These contact pads are sandwiched in between two parylene layers. The entire assembly is less than 20 microns thick. Details of the fabrication process can be found in previous articles [10][11]. The actuators are placed behind the leading edge where the perturbation of the airflow can lead to significant aerodynamic effect. It is believed that this location is the area where the development of the leading edge vortex can be most affected throughout the flapping cycle. The check-valve actuators are mounted such that they are closed during the downstroke and open on the upstroke when not powered. When powered, they remain closed during the upstroke. All the actuators are wired to turn on or off in unison, effectively making them a single actuator. There are approximately five actuator die per wing, resulting in a maximum of 80 check-valves per wing. The actuation voltage was 350V. The wings have a 7 cm span and 3 cm chord.

Figure 9: Wing with integrated MEMS checkvalve electrostatic actuators

As shown in Figure 11, the maximum lift peak occurs at the beginning of the downstroke (0-0.5) while the next lower peak is near the middle of the upstroke (0.5-1.0). The vortex that forms underneath the wing during beginning of

the upstroke contributes to the negative lift portion. Similarly, the results show that the maximum thrust is not produced until almost at the end of the downstroke which is the time when the flexible trailing edge begins to snap down. It is also the time when the separation vortex is being shed.
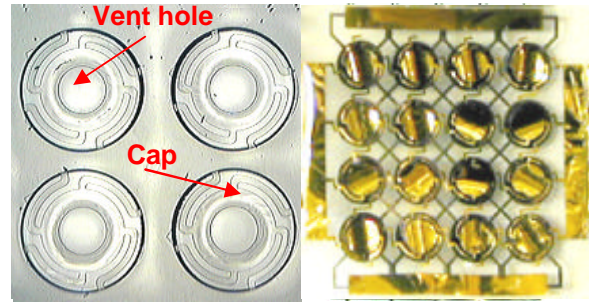

Figure 10: Detailed view of checkvalves (left) and in actuator array. Each actuator is approx 1mm^2
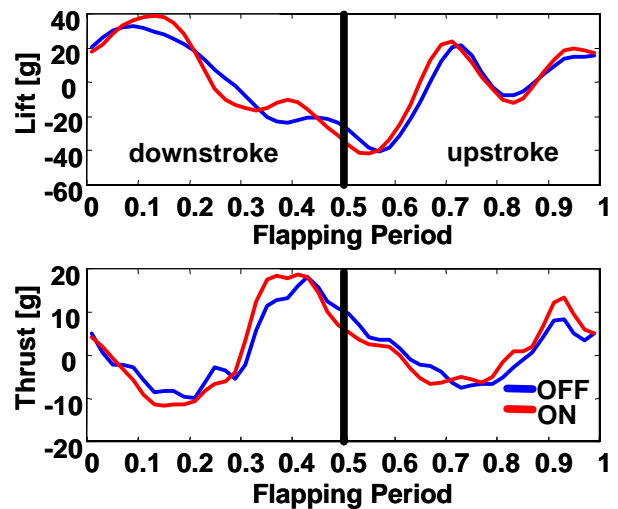

Figure 11: Phased averaged lift and thrust for integrated MEMS checkvalve wing. $J = 0.48$

Observing Figure 11, the actuator effect is obvious from the plots of lift and thrust. The highest lift and thrust peak values (approximately 40 and 20 g, respectively) occur during the actuators are turned on. When the actuators are 'ON' both lift and thrust differ up to 50% at a given instant in time in comparison to the 'OFF' value, which clearly indicates the effect of the valve. The valves *locally* manipulate the unsteady leading-edge vortex and change the pressure distribution on the

wings. It was also observed that as *J* decreases, i.e., flow unsteadiness rises, lift and thrust rose due to growth in the size and strength of the vortex, allowing the actuators to become more effective.

There were correspondingly large average percentage changes over one flapping cycle, as seen in Table 1. There is a 31% increase in mean lift and a 17% boost in mean thrust over the nonactuated wing. Interestingly, these gains come from pure actuation without any sort of feedback control loop in place and with digital (on-off) type actuators. It would be interesting in the future to explore the effect of feedback control and more analog type actuators (half on, full on, full off, etc.) to see if even more improvement can be achieved.

	ON	OFF	%Change
Lift [g]	0.63	0.48	+31%
Thrust [g]	1.17	1.00	+17%

Table 1: Mean lift and thrust for cambered active-valve integrated MEMS wing

4.2 Instantaneous angular speed variation

We controlled the rotational speed of the DC motor driving the wing flapping assembly to achieve *global* control of the unsteady leading edge vortex over the entire wing. The DC motor operates in the linear regime (the wing flapping frequency increases linearly with voltage input to the motor) and there is no motor slip in this mode of operation. A constant DC input voltage creates a constant wingtip velocity. By varying the motor input voltage, the instantaneous angular wingtip velocity is now free to accelerate or decelerate. In order to compare the results of changing the angular speed to the constant speed case, the flapping period remains fixed. Hence, angular speed control really means the tailoring the relative downstroke and upstroke times. For example, the wing might beat faster on the downstroke and slower on the upstroke.

A plain ('reference', i.e., no integrated actuators) wing flapping at *J* = 0.48 is tested and Figure 12 shows the phase average results while

Table 2 lists the quantitative change in lift and thrust over one flapping period. In Figure 12, OFF refers to constant DC voltage input and ON means varying the drive signal. In this example the drive signal was a 20 Hz sine wave with an amplitude of 1 volt and a DC offset equal to the constant DC voltage for the OFF case.
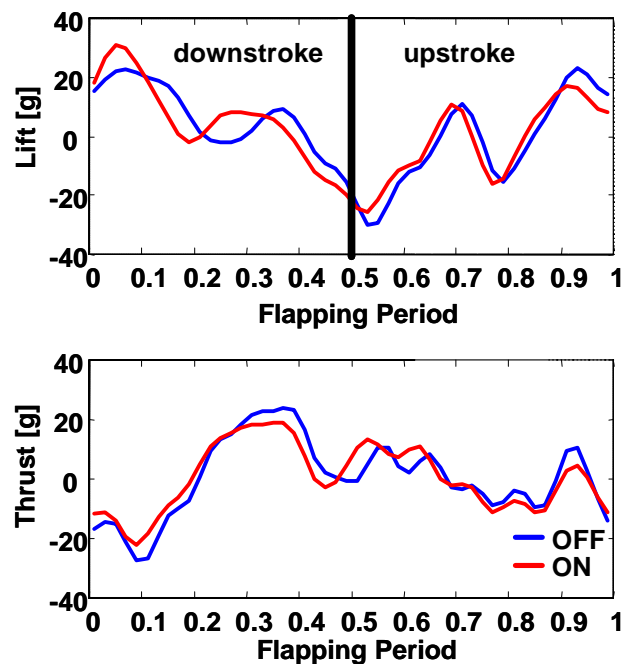

Figure 12: Phase averaged lift and thrust for angular speed control of reference wing, *J* = 0.48.

Table 2 shows that simple variation in the motor drive signal can cause significant changes in the lift and thrust (-8% for lift and +26% for thrust). However, this system is not optimized and there is no feedback control. The next step is to find the appropriate feedback controller for this nonlinear system and to apply it to this actuation method.

	ON	OFF	%Change
Lift [g]	1.78	1.94	-8%
Thrust [g]	0.48	0.38	+26%

Table 2: Mean lift and thrust for angular speed control of reference wing

5 Gur Game feedback controller

Since the system is highly nonlinear and the presence of many MEMS actuators yields the possibility of a large distributed system, we opted not to use a traditional linear quadratic Gaussian or PID controller. Instead, the Gur Game feedback controller was selected. Much like a genetic algorithm or neural net control algorithm, the Gur Game aims for self-organization and self-optimization of the system [12][13]. The essence of the Gur Game is a random walk that is strongly biased toward the global optimum. The key concept in the Gur Game is the global figure of merit, called the reward function, which measures the performance of the system as a whole. The reward function maps the system state from 0 to 1, with higher system performance corresponding to values nearer to 1. At each iteration through the control loop, the reward function is evaluated. Then each actuator is changed probabilistically according to the reward function value. For example, suppose there are two actuators and the reward function value is 0.7. Then for each actuator a random uniform number from 0 to 1 is chosen and compared to the value of the reward function. If the random number is less than the value (0.7 in this case), the actuator changes state in a prescribed manner. If it is greater than 0.7, the actuator remains in the same state. This process is repeated for each actuator and at each iteration. Eventually a global optimal state is achieved.

The advantages of the Gur Game are that is can achieve a globally optimally state with many distributed actuators without having to explicitly dictate the operation of each actuator. The actuators self-organize and self-optimize based on the reward function. The reward function can be virtually of any shape; multi-modal, discontinuous, nonasymptotic, etc. This framework provides for a very general and robust distributed control method.

5.1 Angular speed feedback control

The Gur Game controller has been used in conjunction with the angular speed control concept as discussed previously (see Figure 12). Again, the reward function was based on increasing C_L/C_T. In this example, a square wave signal drives the DC motor and the signal is synchronized with the start of the downstroke by an external trigger. The transmission mechanism interrupts a laser beam and sets the trigger. The amplitude and DC offset of the square wave are 1.0 volts and 4.8 volts, respectively. The controller, however, is free to change the duty cycle of the square wave from 0 to 0.6 in steps of 0.1. A value of 0.5 corresponds to 50% duty cycle. The controller is turned on at T = 20 seconds and turned off at T = 100 seconds. The system state is measured every second. Reference wings at an advance ratio of $J = 0.6$ were tested.
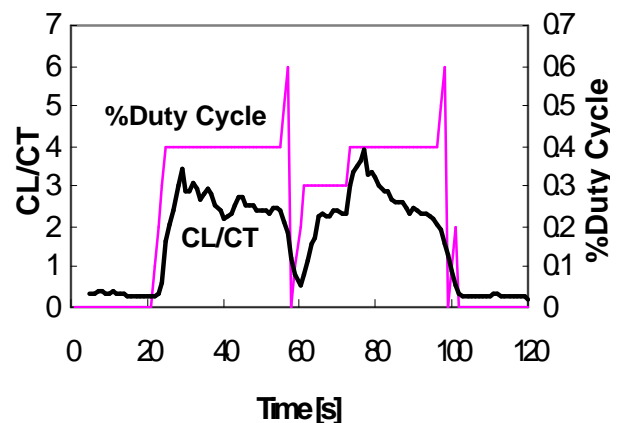

Figure 13: Duty cycle optimization using the Gur Game controller and angular speed variation

As seen in Figure 13, turning on the controller at T = 20 quickly increases the C_L/C_T and soon it reaches a value of 3, which is greater than 300% of the non-controlled value of 0.8, and converges to a duty cycle value of 0.4. But because the Gur Game continually searches for new maxima, it changes the duty cycle and C_L/C_T plummets, as observed around T = 60. The Gur Game then recovers the original optimal duty cycle and C_L/C_T again reaches 3 before the controller is turned off at T = 100. This example demonstrates the robustness and search capabilities of the control scheme.

Tests of control and optimization for two variables were also conducted. Figure 14 illustrates the results of optimizing both the duty

cycle and signal amplitude of a square wave drive input. The experimental conditions are the same as for the previous case but this time both the amplitude of the signal and the duty cycle are varied simultaneously. The signal amplitude ranges from 0 to 0.7 volts and the duty cycle goes from 0 to 0.7 in steps of 0.1. Again, C_L/C_T is the reward function variable and the controller turns on at T = 20 and off at T = 100 seconds.
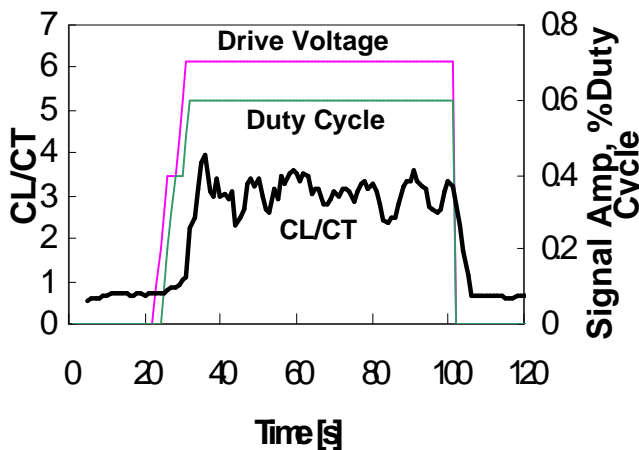

Figure 13: Two variable optimization using the Gur Game controller and angular speed variation

The controller again quickly converges on and remains at an optimal state of 0.7 for the signal amplitude and 0.6 for the duty cycle. The rise in C_L/C_T is 300%, matching the best case achieved with single variable control and optimization.

6   Summary

The unsteady leading edge vortex and the stiffness distribution of the wing were shown to dominant the lift and thrust production for flapping flight. In particular, the growth of a stable separation bubble atop the wing during the downstroke appears to be the mechanism to explain the high unsteady lift coefficients found for flapping fliers in forward flight. The stiffness distribution plays major roles in both lift and thrust generation. A wing that is stiff in the spanwise direction near the leading edge is advantageous in terms of lift in the unsteady flow domain, while one that spanwise flexible

causes a sharp drop in lift for unsteady conditions. In terms of thrust, experiments indicate that a combination of the wing stiffness and how the unsteady leading edge vortex is shed from the inboard wing region determines the final thrust output.

Active flow control for flexible flapping wings has also been demonstrated. Local vortex control of the unsteady leading edge vortex was achieved with mesoscale electrostatic checkvalves fabricated directly on the wing membrane using MEMS techniques. These checkvalve actuators modified the local pressure field near the leading edge by being open or closed during the upstroke and downstroke. Tests measured percent changes in mean lift and thrust over one flapping cycle of 31% and 17%, respectively.

The ability of change the instantaneous angular speed of the wing via varying the voltage signal to the DC motor driving the flapping transmission provided global vortex control. Changing the overall wing motion unmistakably alters both the growth of the unsteady leading vortex, the wing deformation during the flapping cycle, and the shedding of the vortex. In order to demonstrate closed loop control using this actuation method, a control algorithm capable of dealing with this highly nonlinear system required development. This led to research into the Gur Game, an algorithm for self-optimization and self-organization over a wide range of possible systems.

The Gur Game proved itself capable of significantly altering the aerodynamic performance of the wings using simple variation of the drive signal. Over 300% changes in CL/CT ratios were achieved using single and double variable optimization and control. Future work would include expanding the Gur Game to control the distributed MEMS actuators on the wing, thus operating with both local and global closed loop control.

References

[1] Spedding G.R. and Lissaman P.B.S. Technical aspects of microscale flight systems. *J. Avian Biol.*, 29, pp 458-468, 1998.

[2] Dickinson M.H., Lehmann F.-O. and Sane S.P. Wing rotation and the basis of insect flight. *Science*, 284, pp 1954-1960, 1999.

[3] Ellington C.P., Van Den Berg C., Willmott A.P. and Thomas A.L.R. Leading-edge vortices in insect flight. *Nature*, 384, pp 626-630, 1996.

[4] Maxworthy T. Experiments on the Weis-Fogh mechanism of lift generation by insects in hovering flight. Part 1. Dynamics of the 'fling'. *J. Fluid Mech.*, 93, pp 47-63, 1979.

[5] Van Den Berg C. and Ellington C.P. The three-dimensional leading-edge vortex of a hovering model hawkmoth. *Phil. Trans. R. Soc. Lond. B*, 353, pp 329-340, 1997.

[6] Weis-Fogh T. and Jensen M. Biology and physics of locust flight, I-IV. *Phil. Trans. R. Soc. Lond. B*, 239, pp 415-584, 1956.

[7] Bennet A.G., Obye R.C. and Jeglum P.M. "Ornithopter aerodynamic experiments" in: *Swimming and flying in nature*. Ed. Wu, Brokaw and Brennen. Vol. 2, Plenum Press, New York, 1975.

[8] Gu W., Robinson O. and Rockwell D. Control of Vortices on a Delta Wing by Leading-Edge Injection. *AIAA Journal*, Vol. 31, No. 7, pp 1177-1186, 1992.

[9] McCormick S. and Gursul I. Effect of Shear-Layer Control on Leading-Edge Vortices. *J. Aircraft*, Vol 33, No. 6, pp.1087-1093, 1996.

[10] Liger M., Pornsin-Sirirak N., Tai Y.-C., Ho S. and Ho C.-M. Large-area electrostatic-valved skins for adaptive flow control on ornithopter wings. *Solid State Sensor, Actuator, and Microsystems Workshop*, Hilton Head Island, South Carolina, pp 247-250, 2002.

[11] Pornsin-Sirirak N. *Parylene MEMS Technology*. PhD Thesis. California Institute of Technology, 2002.

[12] Tung B. and Kleinrock L. Using finite-state automata to produce self-optimization and self-control. *IEEE transactions on parallel and distributed systems*. Vol. 7, No. 4, pp 439-448, 1996.

[13] Tung B. *Distributed control using finite state automata*. PhD Thesis. University of California, Los Angeles, 1994.